

# Journal of Materials Chemistry A

Materials for energy and sustainability

Accepted Manuscript

This article can be cited before page numbers have been issued, to do this please use: S. Xue, N. Shi, Y. Wan, Z. Xu, D. Huan, S. Zhang, C. Xia, R. Peng and Y. lu, *J. Mater. Chem. A*, 2019, DOI: 10.1039/C9TA07027C.



This is an Accepted Manuscript, which has been through the Royal Society of Chemistry peer review process and has been accepted for publication.

Accepted Manuscripts are published online shortly after acceptance, before technical editing, formatting and proof reading. Using this free service, authors can make their results available to the community, in citable form, before we publish the edited article. We will replace this Accepted Manuscript with the edited and formatted Advance Article as soon as it is available.

You can find more information about Accepted Manuscripts in the [Information for Authors](#).

Please note that technical editing may introduce minor changes to the text and/or graphics, which may alter content. The journal's standard [Terms & Conditions](#) and the [Ethical guidelines](#) still apply. In no event shall the Royal Society of Chemistry be held responsible for any errors or omissions in this Accepted Manuscript or any consequences arising from the use of any information it contains.

## ARTICLE

## Novel carbon and sulfur tolerant anode material $\text{FeNi}_3@ \text{PrBa}(\text{Fe}, \text{Ni})_{1.9}\text{Mo}_{0.1}\text{O}_{5+\delta}$ for IT-SOFCs

Received 00th January 20xx,  
Accepted 00th January 20xx

Shuangshuang Xue,<sup>a</sup> Nai Shi,<sup>a</sup> Yanhong Wan,<sup>a</sup> Zheqiang Xu,<sup>a</sup> Daoming Huan,<sup>a</sup> Shaowei Zhang,<sup>a</sup>  
Changrong Xia,<sup>a</sup> Ranran Peng,<sup>\*a,b,c</sup> Yalin Lu<sup>\*a,b,c,d</sup>

DOI: 10.1039/x0xx00000x

Suppression of carbon deposition and sulfur poisoning without sacrificing electrochemical performance is crucial for operating solid oxide fuel cells (SOFCs), especially in intermediate temperatures (IT). In this work, nickel doped A-site deficiency perovskite oxides  $(\text{PrBa})_{0.95}\text{Fe}_{1.9-x}\text{Ni}_x\text{Mo}_{0.1}\text{O}_{6-\delta}$  (PBFMNix,  $x=0, 0.1, 0.2, 0.3, 0.4$ ) are synthesized and investigated as potential anodes for IT-SOFCs. With the increased contents of  $\text{Ni}^{2+}$ , the ratios of  $\text{Fe}^{2+}/\text{Fe}^{3+}$  and  $\text{Mo}^{5+}/\text{Mo}^{6+}$  in as-prepared PBFMNix reduce continuously under a charge compensating mechanism, which simultaneously depresses the formation of impurity phase ( $\text{BaMoO}_4$ ). Interestingly, the substitution of  $\text{Ni}^{2+}$  benefits the reduction of  $\text{Fe}^{3+}$  to  $\text{Fe}^{2+}$  and  $\text{Mo}^{6+}$  to  $\text{Mo}^{5+}$ , and small portions of Fe and Ni elements are exsolved from the parent oxides forming  $\text{FeNi}_3$  alloy nano-particles, which greatly accelerates chemical adsorption and surface reaction kinetics of  $\text{H}_2$ , and thus improves the electrochemical performances of based oxide anodes. Transformation of the electrical conduction from p-type to n-type after reduction is also observed. A very small polarization resistance of  $0.028 \Omega\text{-cm}^2$  at  $750^\circ\text{C}$  is achieved for the cell with PBFMNi0.3 anode. Importantly, fuelled with syngas with 50 ppm  $\text{H}_2\text{S}$ , the maximum power density of the button cell based on PBFMNi0.3 anode and SDC electrolyte supporting configuration can reach  $498 \text{ mW}\text{-cm}^{-2}$  at  $750^\circ\text{C}$  and a long-term stability over 100 hours can be demonstrated with negligible performance decay. All these results indicate that PBFMNi0.3 is a promising high-performance anode material with good coking resistance and sulfur tolerance in intermediate temperatures.

### 1. Introduction

In nowadays, the innovative development of energy conversion and storage systems is becoming an urgent issue to confront the growing energy demands and global ecocrisis<sup>1</sup>. Solid oxide fuel cells (SOFCs) have drawn special attention as a promising clean energy technology thanks to their high energy conversion efficiency and environment-friendly operation<sup>2</sup>. To increase the volume energy density and the storage and transport safety of fuels, numerous carbon-containing fuels, including coal-derived syngas<sup>3</sup>, ethanol<sup>4, 5</sup>, natural gas<sup>6</sup>, biogas<sup>7</sup>, and wood-derived gases<sup>8</sup> have been applied in SOFCs as substitutes for traditional  $\text{H}_2$  fuel. Moreover, the application of carbon-containing fuels may bring forth other commercial advantages. For example, direct utilization of coal-derived syngas (containing  $\text{H}_2$ ,  $\text{CO}$ ,  $\text{N}_2$ ,  $\text{H}_2\text{O}$ ,  $\text{H}_2\text{S}$ ...) can greatly simplify the purification equipment (compared with those for  $\text{H}_2$ ), increase the

energy conversion efficiency and economic benefit of coal, and reduce the operational cost of power generation. Unfortunately, severe catalytic poisoning and coke deposition occur when applying these coal-derived syngas in traditional Ni-based anodes. This should be ascribed to the unfavourable reactions of Ni with sulfur<sup>9, 10</sup> and the strong catalytic activity of Ni toward carbon formation, which results in serious performance degradation of the anodes and thus the service life reduction of SOFCs. In particular, when operating at the goal temperatures (intermediate temperatures, typically  $600\text{--}750^\circ\text{C}$ ) of SOFC stacks<sup>11, 12</sup>, sulfur poisoning and coke formation over Ni-based anodes are more grievous than those at high temperatures<sup>13, 14</sup>. Therefore, exploring suitable anode materials with good carbon and sulfur tolerance is the key for practical application of SOFCs.

Significant efforts on developing carbon and sulfur tolerant anodes have been focused on mixed conducting perovskite-based materials, such as  $\text{La}_{0.75}\text{Sr}_{0.25}\text{Cr}_{0.5}\text{Mn}_{0.5}\text{O}_{3-\delta}$  (LSCM)<sup>15</sup>,  $\text{La}_{1-x}\text{Sr}_x\text{Cr}_{1-x}\text{Fe}_x\text{O}_{3-\delta}$  (LSCrF)<sup>16</sup>,  $\text{La}_{0.2}\text{Sr}_{0.8}\text{TiO}_3$  (LST)<sup>17</sup>, and double perovskite oxides such as  $\text{Sr}_2\text{Fe}_{1.5}\text{Mo}_{0.5}\text{O}_{6-\delta}$  (SFM)<sup>18</sup>,  $\text{PrBaMn}_2\text{O}_{5+\delta}$  (PBM)<sup>19, 20</sup>. However, these alternative perovskite-based anodes typically exhibit insufficient electro-catalytic activity for fuel oxidation. Recently, adding a second metal which will be *in-situ* exsolved from oxides as nano-metal particles has been intensively studied to optimize perovskite anode catalysts in SOFCs<sup>21-25</sup>. Much energy have been invested to decorate Fe-based perovskite oxides using Ni or Co substitute, such as  $\text{LaSrFeNiO}_{6-\delta}$  (LSFN)<sup>26</sup>,  $\text{Pr}_{0.4}\text{Sr}_{0.6}\text{Co}_{0.2}\text{Fe}_{0.7}\text{Nb}_{0.1}\text{O}_{3-\delta}$  (PSCFN)<sup>27</sup>. It was found that the exsolved second metal (Ni, Co...) can form a bimetallic alloy with the host metal (Fe), and thus synergistically promote the

<sup>a</sup> CAS Key Laboratory of Materials for Energy Conversion, Department of Materials Science and Engineering, University of Science and Technology of China, Hefei, 230026 Anhui, China.

<sup>b</sup> Synergetic Innovation Center of Quantum Information & Quantum Physics, University of Science and Technology of China, Hefei, Anhui 230026, China.

<sup>c</sup> Hefei National Laboratory of Physical Science at the Micro-scale, University of Science and Technology of China, Hefei, 230026 Anhui, China.

<sup>d</sup> National Synchrotron Radiation Laboratory, University of Science and Technology of China, Hefei 230026, P. R. China.

<sup>e</sup> \* Corresponding author.

<sup>f</sup> Electronic Supplementary Information (ESI) available: [Rietveld refinement parameters, the change in PO<sub>2</sub> in ECR experiments, conductivity results, ECR theory and results, electrochemical stability results and SEM results]. See DOI: 10.1039/x0xx00000x

catalysts' catalytic activity and remarkably enhance the resistance to carbon accumulation and sulfur poisoning<sup>26</sup>. Unfortunately, these studies are mainly confined in operating at high temperatures (800–900 °C) for lacking of sufficient catalytic activities toward carbon-containing fuels in intermediate temperatures, which is more prone to occur severe carbon deposition and sulfur poisoning.

In this work, we prepared nickel doped A-site deficiency perovskite oxides  $(\text{PrBa})_{0.95}\text{Fe}_{1.9-x}\text{Ni}_x\text{Mo}_{0.1}\text{O}_{6-\delta}$  (PBFMNix,  $x=0-0.4$ ) with the aim of improving the electrochemical activity of anode materials and enhancing its resistance to carbon deposition and sulfur poisoning at intermediate temperatures (550–750 °C). Mo elements with high and changeable valences were introduced into B-site to stabilize Fe-based perovskite lattices<sup>28</sup> and to contribute to their electronic conductivities in reducing atmosphere. Thus, the crystal structures, valence states of B-site elements and conductivities of the series samples were explored before and after reduction. Surface adsorption kinetics of these samples in reducing atmosphere were also explored as functions of Ni contents and temperatures. Electrochemical performances and stabilities of single cells using these anodes were investigated with fuels like wet hydrogen, wet syngas ( $\text{H}_2$ :  $\text{CO}=2:1$ ), syngas with 50 ppm  $\text{H}_2\text{S}$  and wet propane.

## 2. Experimental sections

### 2.1 Powders synthesis

$(\text{PrBa})_{0.95}\text{Fe}_{1.9-x}\text{Ni}_x\text{Mo}_{0.1}\text{O}_{6-\delta}$  (PBFMNix,  $x=0-0.4$ ) powders were synthesized using a citric acid - ethylene diaminetetraacetic acid (EDTA) complexing method. Stoichiometric amounts of  $\text{Pr}(\text{NO}_3)_3 \cdot 6\text{H}_2\text{O}$ ,  $\text{Ba}(\text{NO}_3)_2$ ,  $\text{Fe}(\text{NO}_3)_3 \cdot 9\text{H}_2\text{O}$ ,  $\text{Ni}(\text{NO}_3)_2 \cdot 6\text{H}_2\text{O}$ , and  $(\text{NH}_4)_6\text{Mo}_7\text{O}_{24} \cdot 4\text{H}_2\text{O}$  were dissolved in deionized water. Citric acid and EDTA were added to the solution as the complexing agents and fuels with a molar ratio of citric acid: EDTA: metal cations = 1.5: 1: 1. The pH value of the solution was adjusted to 7 with ammonia. After being stirred for 2 hours, the solution was heated in a microwave oven until self-ignition. The combustion ashes were heat-treated at 1100 °C for 6 hours in air to form the desired PBFMNix powders. PBFMNix powders were reduced in wet  $\text{H}_2$  at 800 °C for 10 hours to *in-situ* exsolute Ni-based nano-particles. Powders of  $\text{Sm}_{0.2}\text{Ce}_{0.8}\text{O}_{1.9}$  (SDC) electrolyte were prepared with carbonate co-precipitation method, described previously<sup>29,30</sup>, using  $\text{Ce}(\text{NO}_3)_3 \cdot 6\text{H}_2\text{O}$  (99%) and  $\text{Sm}(\text{NO}_3)_3 \cdot 6\text{H}_2\text{O}$  (99.95%) as the precursors.  $\text{La}_{0.6}\text{Sr}_{0.4}\text{Co}_{0.2}\text{Fe}_{0.8}\text{O}_{3-\delta}$  (LSCF) powders were synthesized via a solution combustion method as described elsewhere<sup>31</sup>. All the raw chemicals were purchased from Sinopharm Chemical Reagent Co. Ltd.

### 2.2 Cell fabrication

Single cells with the structure of PBFMNix–SDC|SDC|LSCF–SDC were prepared taking electrolyte supporting configurations. SDC electrolyte substrates with a thickness of about 200  $\mu\text{m}$  were prepared by dry-pressing 0.15 g SDC powders uniaxially at 200 MPa, followed by sintering at 1450 °C for 5 hours in air. PBFMNix and SDC powder mixtures (weight ratio of 7:3) were blended with  $\alpha$ -terpinol in weight ratio of 1:1.5 to form anode ink, which was then applied onto one surface of SDC electrolyte by a screen-printing method. After drying at 80 °C for 60 min, the cathode ink containing LSCF and SDC powders (weight ratio of 6:4) was applied onto the other surface

of the SDC electrolyte via the same method. The samples were co-fired at 1000 °C in air for 2 hours to complete the fabrication process. Thickness of each electrode was about 20  $\mu\text{m}$  (Figure. S10). As comparison, NiO–SDC (6:4) |SDC|LSCF–SDC (6:4) cells were also prepared via the same process.

### 2.3 Characterization of powders

Room temperature X-ray diffraction (RT-XRD) patterns of the series samples were recorded on a Rigaku D/Max 2100 powder X-ray diffractometer with  $\text{Cu-K}\alpha$  radiation ( $\lambda = 1.5418 \text{ \AA}$ ) at a scan rate of 3  $\text{deg min}^{-1}$  in the range of 20–80 °. Rietveld refinements were conducted with the program FullProf to determine the space group and the lattice parameters. High-resolution transmission electron microscopy (HRTEM), scanning transmission electron microscopy (STEM) and corresponding energy dispersive spectroscopy (EDS) analyses were performed on a JEOL JEM-ARM200F TEM/STEM with a spherical aberration corrector.  $\text{H}_2$ -temperature programmed reduction (TPR) experiments were conducted on 0.05 g PBFMNix ( $x=0-0.3$ ) using a Thermo Finnigan TPDRO 1100 apparatus equipped with a thermal conductivity detector. The flow rate of 5%  $\text{H}_2/\text{Ar}$  for TPR analysis was 20  $\text{ml min}^{-1}$ , and the temperature ramp rate was 10  $^\circ\text{C min}^{-1}$ . X-ray photoelectron spectroscopy (XPS) analysis was performed using a Kratos Analytical AXIS 165 with a monochromatic Al  $\text{K}\alpha$  source to investigate the oxidation states of powder samples. A nonlinear Shirley-type background method was used to analyse the core peaks. In the fitting, the peak positions and areas were optimized via the Lorentzian–Gaussian method. Morphology of the powders was characterized using a SEM (JSM-6700F).

### 2.4 Characterization of cells

Electrochemical performances of cells were characterized in a home-developed testing system using multiple fuels such as hydrogen, propane, syngas ( $\text{H}_2$ :  $\text{CO}=2:1$ ) and syngas with 50 ppm  $\text{H}_2\text{S}$ . The flow rates of the gases were set as  $\sim 50 \text{ ml min}^{-1}$ . Ambient air was used as the oxidant. Before electrochemical testing in propane and syngas containing fuels, wet 5%  $\text{H}_2/\text{Ar}$  was injected into anode area at 800 °C for 2 hours to reduce PBFMNix anodes. A.C. impedance spectra and electrochemical performances of the cells were investigated from 750 down to 550 °C using an electrochemistry workstation (Garmary framework) in the typical frequency range of 0.01 Hz  $\sim$  1 MHz with the AC voltage amplitude of 10 mV. Polarization curves were obtained by performing linear sweep voltammetry from open circuit potential to 0.2 V with a scan rate of 50  $\text{mV s}^{-1}$ . Fractured microstructures of the cells were characterized using a scanning electron microscopy (SEM, JSM-6700F).

### 2.5 Electrical performance evaluation

Electrical conductivity relaxation (ECR) measurements were performed using a standard 4-probe technique to study the oxygen transport kinetics of samples in reducing atmospheres. For this measurement, PBFMNix powders were mixed with 5% PVA (polyvinyl alcohol) by ball-milling for 2 hours. The powder mixtures were uniaxially pressed at 300 MPa and then sintered in air at 1350 °C for 10 hours to obtain rectangular bar samples with dimensions about 32.0  $\times$  4.5  $\times$  0.56  $\text{mm}^3$ . The surface SEM images of the sintered samples were presented in Figure. S8 and the densities of the sintered samples measured by Archimedes method were all above

96% of their theoretical ones. Electrical connections to the samples were established by four silver wires, and silver conducting resin was used to enhance the contact between the specimen and the Ag wires. Before ECR experiments, the bar samples were firstly annealed in 5% H<sub>2</sub>/Ar at 800 °C for 10 hours to ensure the steady states of samples. Conductivities of specimen were measured as a function of time following a step-wise decrease of oxygen partial pressure performed by switching the gas stream from humidified 5% H<sub>2</sub>/Ar to humidified 10% H<sub>2</sub>/Ar at a total gas flow rate of 200 ml min<sup>-1</sup> and the resulting changes in oxygen partial pressures (P<sub>O<sub>2</sub></sub>) at different temperatures were shown in Table. S2.

### 3. Results and discussion

#### 3.1 In-situ formation of nano-metal particles

Figure. 1a shows the RT-XRD spectra of the as-prepared PBFMNix (x=0, 0.1, 0.2, 0.3, 0.4) powders calcined at 1100 °C for 6 hours in air. Peak at around 26.5 °, indexed as BaMoO<sub>4</sub> (JCPDS#48-0335) is clearly observed in the spectra of as-prepared (PrBa)<sub>0.95</sub>Fe<sub>1.9</sub>Mo<sub>0.1</sub>O<sub>6-δ</sub> (x=0), indicating that pure perovskite structure failed to be obtained in such composition. This should be ascribed to the high oxidation state of Mo<sup>6+</sup> under oxidizing atmosphere, similar to that in famous Sr<sub>2</sub>FeMoO<sub>6-δ</sub>.<sup>32</sup> Substitution of Ni for Fe in PBFMNix has the potential to stabilize the pure-phase perovskite structure in air. With the increasing contents of Ni substitution, peak for BaMoO<sub>4</sub> becomes weaker and gets invisible when the doping contents x reaches above 0.2, exhibiting a pure perovskite structure. X-ray photoelectron

spectroscopy (XPS) investigation suggests that Ni elements show divalent valence state Ni<sup>2+</sup> (~854.7/856.5) (Figure. 2a) in the series samples. And therefore, the substitutions of Fe<sup>3+</sup> by Ni<sup>2+</sup> enables more Mo elements to enter the lattice of perovskites (PBFMNix) under a charge compensating mechanism, and thus inhibits the formation of impurity phase (BaMoO<sub>4</sub>). Moreover, as shown in Figure. 2a, b and c, both Fe and Mo elements demonstrate mixed oxidation states, including Fe<sup>2+</sup> (~709.8 eV) and Fe<sup>3+</sup> (~710.8, 711.6, 713.4, and ~719.2 eV), and Mo<sup>5+</sup> (~231.6 and ~234.7 eV) and Mo<sup>6+</sup> (~232.3 and ~235.4 eV)<sup>31</sup>, respectively. Importantly, the ratios for Fe<sup>2+</sup>/Fe<sup>3+</sup> and Mo<sup>5+</sup>/Mo<sup>6+</sup> in as-prepared PBFMNix (table.1) reduce continuously with the increasing Ni-doping contents, testifying the charge compensating mechanism. It should be also noted that PBFMNix and SDC have good chemical compatibility testified by the XRD patterns for their mixtures calcined at 1000 °C for 2 hours in air (Figure. S1).

For the reduced samples treated at 800 °C in wet H<sub>2</sub> for 10 hours, FeNi<sub>3</sub> alloy (JCPDS#38-0419, Pm-3m, a = 3.545 Å) instead of pure Ni (JCPDS#04-0850, Fm-3m, a = 3.524 Å) was successfully exsolved from parent materials PBFMNix (x=0.2, 0.3, 0.4), as shown in Figure. 1b and c, thus forming FeNi<sub>3</sub>@PBFMNix. The reason why the alloy was not detected in reduced PBFMNi0.1 may be attributed to the low contents of resolved FeNi<sub>3</sub> particles. It is worth noticing that secondary impurity phase of PrO<sub>x</sub> appeared when the doping amounts of Ni reached 0.4, indicating that perovskite structure has been partially destroyed due to the severe Ni-Fe exsolution. This may result in unstable performance when it is used as SOFC anode. Interestingly, BaMoO<sub>4</sub> impure phase existed in PBFMNix (x = 0, 0.1,

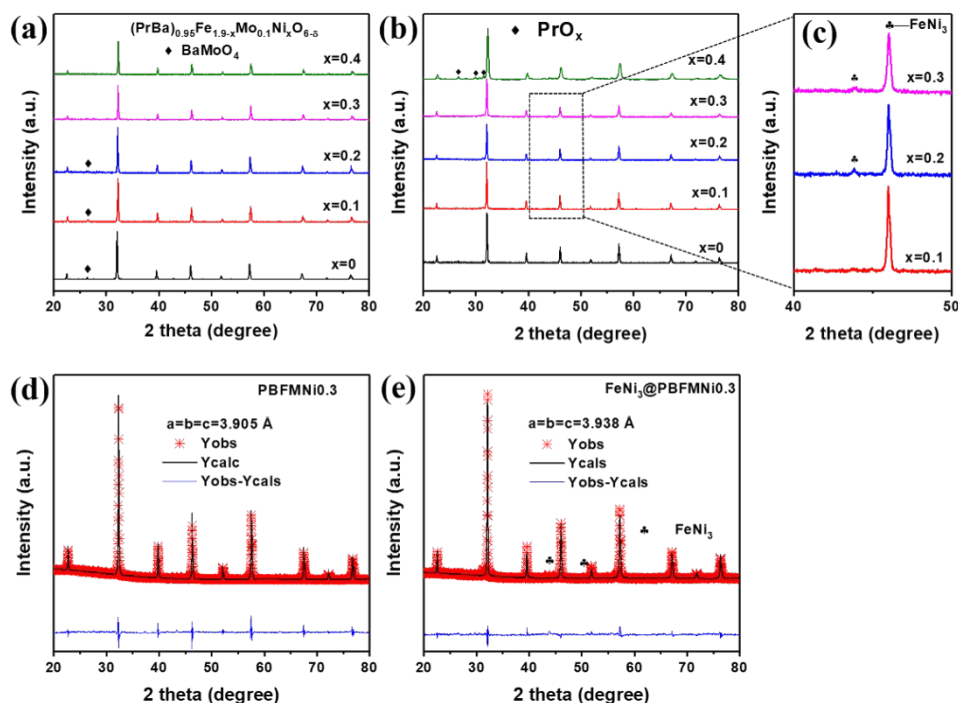


Figure. 1 Room-temperature XRD patterns of (a) as-prepared PBFMNix (x =0-0.4) powders in air and (b) the reduced PBFMNix (x =0-0.4) powders processed in wet H<sub>2</sub> at 800 °C in the range of 20-80 °. (c) The magnified spectra of (b) in the range of 40-50 °. And Refined XRD profiles for (d) as-prepared and (e) reduced PBFMNi0.3.

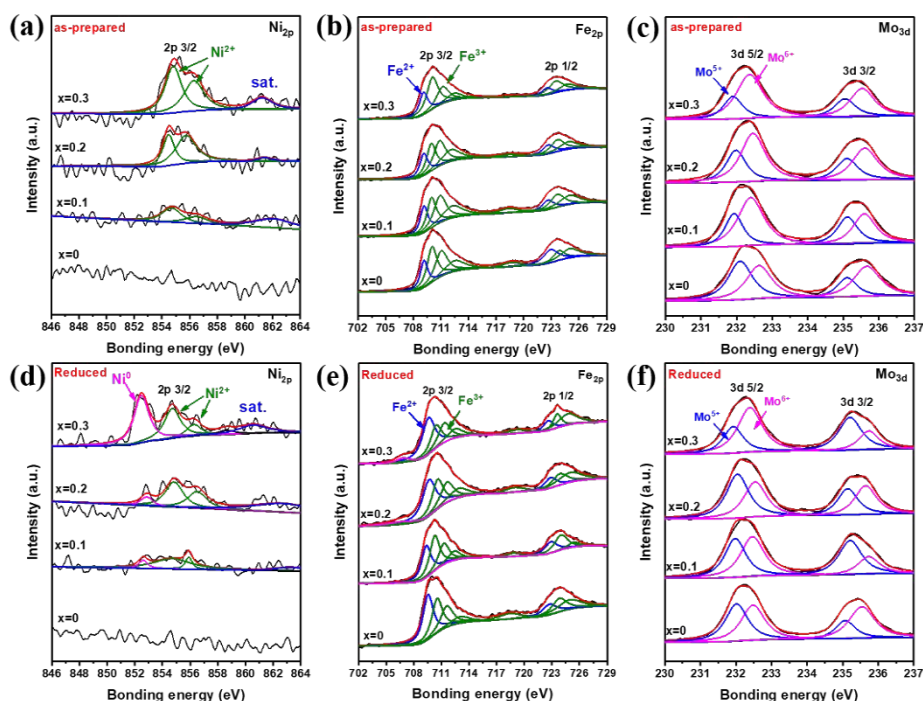


Figure 2 XPS spectra of as-prepared and reduced PBFMNix ( $x=0, 0.1, 0.2, 0.3$ ): (a, d) Ni 2p (b, e) Fe 2p (c, f) Mo 3d

0.2) powders diminished after reduction, which may be ascribed to the lower ratio of  $\text{Mo}^{6+}$  under reducing atmosphere as demonstrated in the XPS fitting results (Table.1). The XPS spectra (Figure. 2d) of the reduced samples further indicate that both metallic nickel  $\text{Ni}^0$  ( $\sim 852.6/858.6$ ) and divalent valence state  $\text{Ni}^{2+}$  ( $\sim 854.7/856.5$ )<sup>32,33</sup> are detected in the reduced samples. As calculated from the fitting results, most of the nickel elements are still in the lattice and only a fraction are reduced to metallic nickel. This seems to suggest that Ni cannot be totally exsolved from the parent oxide, similar to that in  $\text{Sr}_2\text{FeMo}_{0.65}\text{Ni}_{0.35}\text{O}_{3.6}$ <sup>31</sup>. For Fe elements, peaks corresponding to  $\text{Fe}^0$  in addition to mixed oxidation state of  $\text{Fe}^{2+}/\text{Fe}^{3+}$  are clearly observed, as shown in Figure. 2e. The coexistence of Ni and Fe metal spectra confirms the formation of  $\text{FeNi}_3$  alloy.

To obtain an accurate lattice parameter, Rietveld refinements of XRD spectra for as-prepared and reduced PBFMNi0.3 were conducted based on a cubic structure (space group: Pm-3m, No. 221). The refined XRD profiles are shown in Figure. 1c and d, and the

refinement results are summarized in table S1. The lattice constants of as-prepared PBFMNi0.3 powders are  $a=b=c=3.905 \text{ \AA}$ . And after reduction, the oxide lattice expanded to  $a=b=c=3.938 \text{ \AA}$  due to the formation of more oxygen vacancy along with the increased ionic radius of Fe and Mo ions due to their reduced average valence.

Figure. 3 display the morphology of the formed  $\text{FeNi}_3$ @PBFMNix powders. With no Ni substituting ( $x=0$ ), glossy particle surface is shown; while in case of Ni substituted samples ( $x>0$ ), many small sphere-like particles (15-25 nm) are uniformly distributed on the oxide surface, indicating the formation of  $\text{FeNi}_3$  nano-particles (even for  $x=0.1$ ). Notably, although the amounts of  $\text{FeNi}_3$  particles increase with the Ni contents, the size of particles seems changeless. Scanning transmission electron microscopy (STEM) along with energy X-ray spectroscopy (EDS) analysis was conducted on the  $\text{FeNi}_3$ @PBFMNi0.3 powders to further confirm the composition of the formed small particles. As clearly shown in the STEM and elemental EDS mapping images (Figure. 4a), both Ni and Fe elements are present in these small particles, confirming the exsolution of Ni-Fe alloy nano-particles on the surface of the PBFMNi0.3 particles. This is consistent with XRD and XPS analysis. High resolution transmission electron-microscopy (HRTEM) pictures of the  $\text{FeNi}_3$ @PBFMNi0.3 powder are shown in Figure. 4b. The lattice space in the sphere-like nano-particle is determined as 0.20 nm, corresponding to the (111) plane of the cubic  $\text{FeNi}_3$  alloy, and for the oxide part, the lattice space is measured as 0.28 nm, in correspondence with the (110) plane of reduced PBFMNi0.3 perovskite structure. All these results clearly demonstrate  $\text{FeNi}_3$  alloy was exsolved from PBFMNix perovskite oxides. It is worth noticing that most Ni elements are still observed in the oxides, as shown in

Table.1 Ratios of Fe 2p and Mo 3d peaks of PBFMNix obtained by X-ray photoelectron spectroscopy

	$\text{Fe}^{2+}/\text{Fe}^{3+}$		$\text{Mo}^{5+}/\text{Mo}^{6+}$	
	As-prepared	Reduce d	As-prepared	Reduce d
$x=0$	0.34	0.53	0.78	0.75
$x=0.1$	0.31	0.48	0.60	1.21
$x=0.2$	0.30	0.50	0.56	1.07
$x=0.3$	0.28	0.51	0.39	0.89

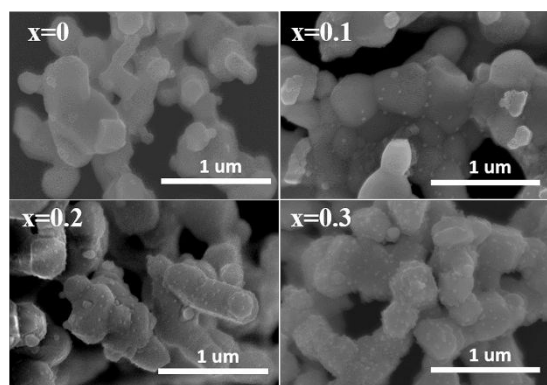


Figure. 3 SEM images of reduced PBFMNix ( $x = 0-0.3$ ) at 800 °C in wet  $H_2$  for 10 hours. Nano-sized  $FeNi_3$  particles (15-25 nm) exsolved from the backbone dispersed uniformly on the reduced oxides surface.

Figure. 4a. This is consistent with the above XPS results. Notably, the exsolved  $FeNi_3$  are embedded to a considerable depth in the parent oxide (Figure. S2), which may depress the carbon formation due to strong interaction between the exsolved socketed particles and the parent oxides<sup>34</sup>.

To figure out the exsolution properties of  $FeNi_3$ , TPR profiles of PBFMNix in a 5%  $H_2/Ar$  gas mixture were conducted, in which the hydrogen consumption was measured as a function of the operating temperatures. As depicted in Figure. 5, PBFMNiO presents one main reduction peak at  $\sim 500$  °C related to the reduction of  $Fe^{3+}$  to  $Fe^{2+}$ <sup>35,36</sup> without the reduction peak of  $Mo^{6+}$  in the perovskite bulk. While for PBFMNix ( $x=0.1-0.3$ ), in addition to the reduction peaks for  $Fe^{3+}$ , two additional peaks locate in  $\sim 630$  and  $\sim 680$  °C can be clearly observed, which should be ascribed to the reduction of  $Mo^{6+}$  to  $Mo^{5+}$ <sup>33</sup> and the formation of  $FeNi_3$ <sup>36,37</sup>, respectively. This is consistent with XPS results that the ratio for  $Mo^{5+}$  hardly changes in PBFMNiO while obviously increases in PBFMNix ( $x=0.1-0.3$ ) before and after

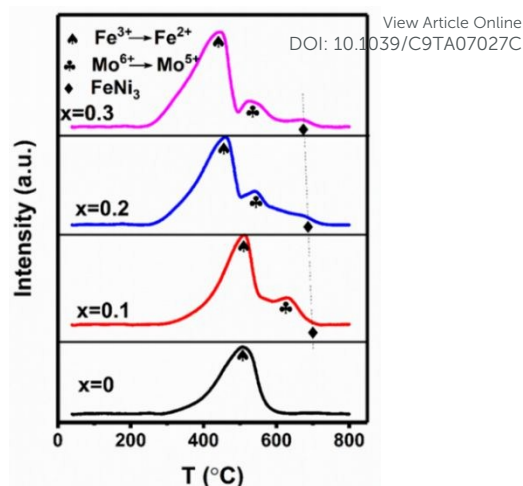


Figure. 5 TPR profiles of PBFMNix ( $x=0-0.3$ ) powders

reduction, and that  $Fe^0$  and  $Ni^0$  peaks appear in XPS spectra of reduced PBFMNix ( $x=0.1-0.3$ ). Moreover, with the increase of Ni substitution ( $x$ ), the reduction peaks for  $Fe^{3+}$  and  $Mo^{6+}$  gradually shift to a lower temperature and the peaks' areas for  $FeNi_3$  alloy formation are obviously improved. This is consistent with the larger peak' areas for  $Ni^0$  and  $Fe^0$  presented in the XPS spectra of reduced samples with more Ni-doping contents (Figure. 2d). These results all indicate that Ni-doping could facilitate the reduction of  $Fe^{3+}$  to  $Fe^{2+}$  and  $Mo^{6+}$  to  $Mo^{5+}$ , and prompt more  $FeNi_3$  metallic nano-particles generated.

### 3.2 Conductivity

As shown in Figure.6a, the conductivity plots of all PBFMNix samples exhibit an up-down transition at 500-600 °C, indicating semiconductor behavior at low temperatures (200-500 °C), and metallic behaviour at higher temperatures (550-800 °C). Notably, the electrical conductivities increase with the Ni contents in PBFMNix,

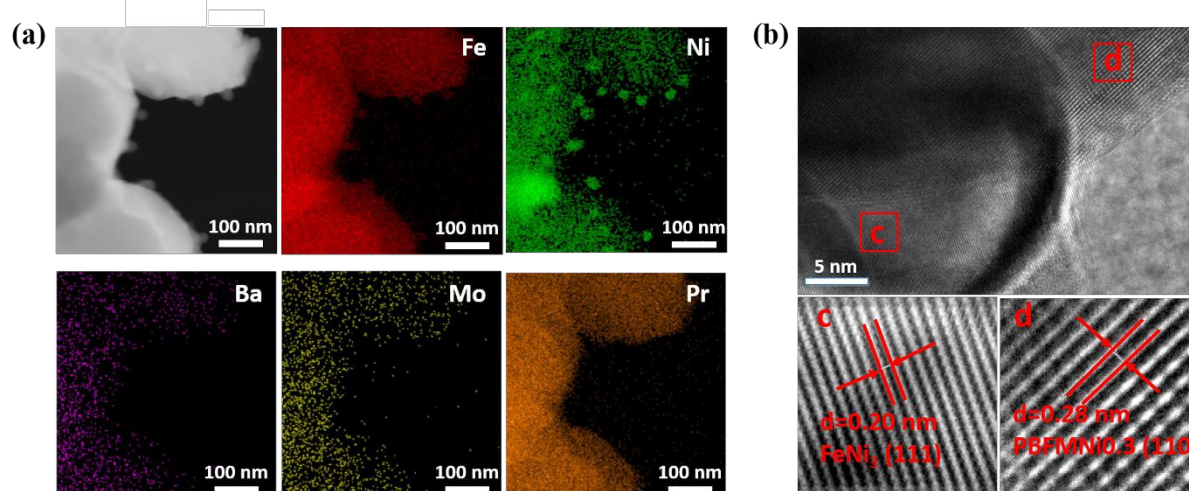
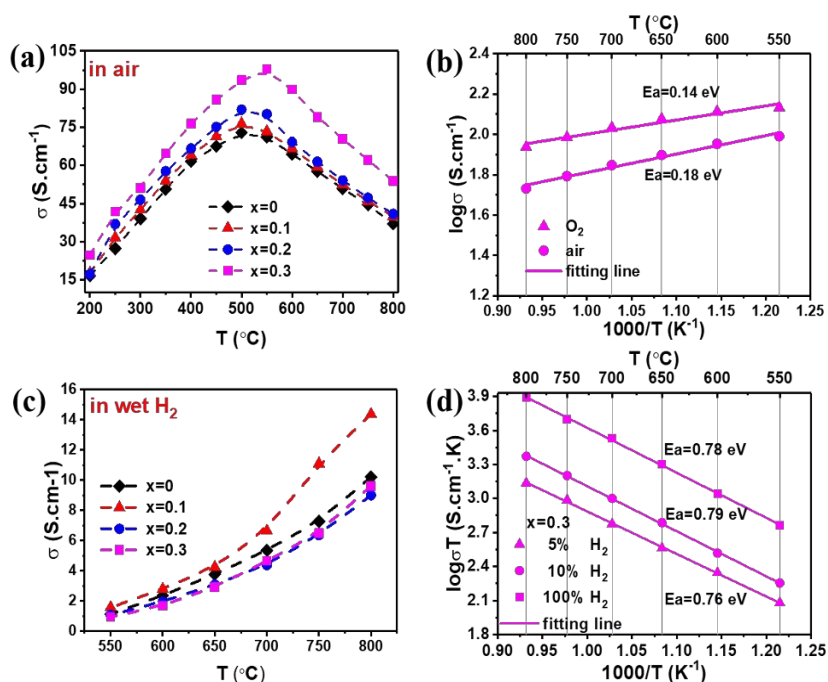


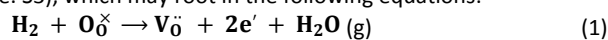
Figure.4 (a) the STEM pictures and the EDS mappings of reduced PBFMNi0.3 powders in HAADF-STEM mode; (b) HRTEM images of a typical reduced PBFMNi0.3 particle and the crystal lattice analyses associated with fast Fourier transformation of  $FeNi_3$  alloy (c region) and PBFMNi0.3 (d region).



View Article Online  
DOI: 10.1039/C9TA07027C

Figure 6 (a) conductivities of PBFMNix ( $x = 0-0.3$ ) in air at 200–800 °C; (b) Arrhenius plots of conductivity at 550–800 °C in  $O_2$  and air for PBFMNi0.3; (c) conductivities of after-reduced PBFMNix ( $x = 0-0.3$ ) in wet  $H_2$  at 550–800 °C; (d) Arrhenius plots of conductivity at 550–800 °C in wet 5%  $H_2/Ar$ , 10%  $H_2/Ar$  and 100%  $H_2$  for PBFMNi0.3, respectively.

suggesting that the doping of Ni could facilitate the conductivities of PBFMNix in air. This may partially result from the less impurity phase formed in Ni substituting samples. Arrhenius plots of conductivity for PBFMNi0.3 measured at 550–800 °C in pure  $O_2$  and air are shown in Figure 6b. The higher conductivities under pure  $O_2$  than that in air suggests that the sample is a p-type conductor. The electrical conductivities of  $FeNi_3@PBFMNix$  ( $x = 0-0.3$ ) formed by annealing PBFMNix in humidified 5%  $H_2/Ar$  at 800 °C for 10 hours were also investigated in the temperature range of 550–800 °C under humidified  $H_2$ . As shown in Figure 6c, all the electrical conductivities increase with the increase of testing temperatures, demonstrating a semiconductor behavior. Interestingly, largest electrical conductivities of  $14.38 S \cdot cm^{-1}$  at 800 °C was achieved at  $x=0.1$ , unlike that measured in air. Arrhenius plots of electrical conductivities for  $FeNi_3@PBFMNi0.3$  in different reducing atmosphere are shown in Figure 6d. The higher conductivity in pure  $H_2$  than that in 5%  $H_2/Ar$  indicating the sample exhibits n-type semiconductor characteristic, different from that of as-prepared PBFMNi0.3. Such transformation of the electrical conduction mechanism from p-type to n-type after reduction also occurred in other two samples PBFMNix ( $x=0.1, 0.2$ ) (Figure. S3), which may root in the following equations:



Where  $H_2$  extracted  $O_0^x$  to form  $H_2O$  with an oxygen vacancy  $V_0^{\cdot\cdot}$  and two electron generated. Therefore, the amount of extrinsic electron in samples after reduction increases and gradually depletes the number of electron hole ( $h^*$ ), which explains why the materials transformed from p-type conductor to n-type conductor. The generated electrons can reduce the valence of B-site elements via following equations:

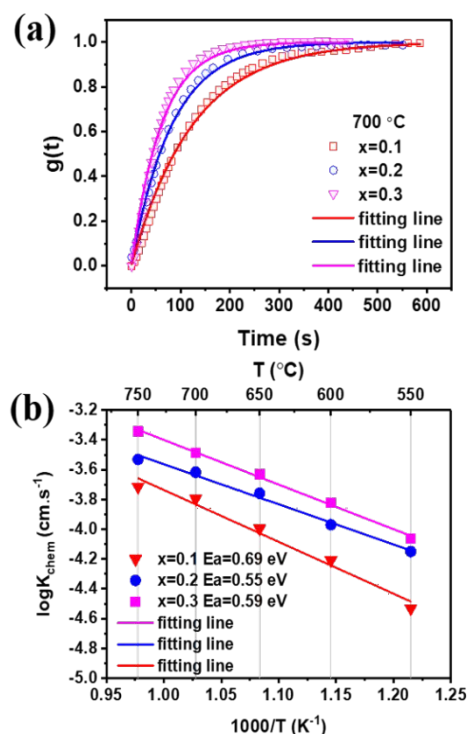
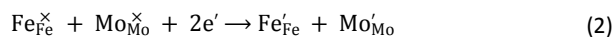


Figure 7 (a) Electrical conductivity relaxation curves of reduced PBFMNix ( $x=0.1, 0.2, 0.3$ ) at 700 °C; (b) Arrhenius plots of the surface exchange coefficient of the three samples at 550–750 °C.



Electrical conductivity is often derived from the exclusive movement of electrons through B-O-B or B-O-B' in perovskites (e.g.  $\text{Fe}^{3+}$  and  $\text{Mo}^{5+}$  pair<sup>38</sup>). As shown in TPR and XPS results, the substitution of  $\text{Ni}^{2+}$  can facilitate the reduction of  $\text{Mo}^{6+}$  and  $\text{Fe}^{3+}$ , and thus improves the electronic conduction. While with the increase of Ni substitution, more alloy  $\text{FeNi}_3$  is formed, which indicates more electrons consumed (equation (3) and (4)), which in turn leads to the depressed electronic conduction. According to the XPS fitting results above (Table. 1), the ratios for  $\text{Fe}^{3+}$  and  $\text{Mo}^{5+}$  electronic configuration in the series reducing samples reach its maximum value when the Ni contents reaches 0.1, which corresponds well with the maximum electronic conductivity of  $x=0.1$  among these reduced samples. Meanwhile, the conductivity activation energies of these samples under  $\text{H}_2$  are much higher than that in air. The high activation energies in the reduced system imply electrons are more localized and electronic conduction occupy smaller proportion in total conductivity.

### 3.3 Surface adsorption kinetics

ECR technique was used to evaluate the the surface oxygen exchange properties of  $\text{FeNi}_3@\text{PBFMNix}$  in a humidified  $\text{H}_2/\text{Ar}$  atmosphere at 550-750 °C (see the Experimental section). By abruptly switching the gas from humidified 5%  $\text{H}_2/\text{Ar}$  to humidified 10%  $\text{H}_2/\text{Ar}$ , the oxygen partial pressure ( $P_{\text{O}_2}$ ) decreases sharply from  $1.07 \times 10^{-20}$  atm to  $2.69 \times 10^{-21}$  atm (750 °C, Table. S2). To meet the change of environmental oxygen partial pressure, lattice oxygen of PBFMNix will partially escape from the lattice and react with hydrogen, similar to the redox reaction taking place in the anode of SOFCs. This reaction can be

expressed by equation (1) in Kröger-Vink notation<sup>39</sup>. According to the linear interface kinetics assumption<sup>40,41</sup>, the total surface reaction rate,  $r$  ( $\text{mol}\cdot\text{s}^{-1}$ ), can be expressed as:

$$r = SK_{\text{chem}}[c(t) - c(\infty)] \quad (5)$$

Where  $K_{\text{chem}}$  ( $\text{cm}\cdot\text{s}^{-1}$ ) is the surface reaction rate constant, often referred as the chemical surface oxygen exchange coefficient that can be obtained by the fitting curves of normalized conductivity;  $S$  ( $\text{cm}^2$ ) is the surface area,  $c(t)$  ( $\text{mol}\cdot\text{cm}^{-3}$ ) presents the oxygen concentration at time  $t$ , and  $c(\infty)$  ( $\text{mol}\cdot\text{cm}^{-3}$ ) presents the oxygen concentration in the final equilibrium time. The final equilibrium time reduces with the increase of Ni-doping contents ( $x$ ) in PBFMNix (Figure. 7a), indicating the accelerated  $\text{H}_2$  oxidation process (lattice oxygen reduction process). The time dependences of obtained normalized conductivities in ECR experiments for  $\text{FeNi}_3@\text{PBFMNix}$  ( $x=0.1-0.3$ ) are plotted in Figure. S4 and the corresponding fitting results of  $K_{\text{chem}}$  are plotted in Figure. 7b. Obviously, PBFMNi0.3 shows the largest  $K_{\text{chem}}$  values among the investigated samples, of  $3.25 \times 10^{-4}$  and  $1.50 \times 10^{-4} \text{ cm}\cdot\text{s}^{-1}$  at 700 and 600 °C, respectively. Such enhanced  $K_{\text{chem}}$  can be attributed to more nano-catalysts  $\text{FeNi}_3$  exsolved from the oxides but with changeless particle size, which enlarged triple phase boundary (TPB) length and accelerated the transmission of the charged species<sup>41</sup>.

### 3.4 Electrochemical properties

To assess the electrochemical performance of PBFMNix ( $x=0.1-0.3$ ) anodes, I-V curves of the single cells using PBFMNix-SDC anodes (*in-situ* reducing to  $\text{FeNi}_3@\text{PBFMNix-SDC}$ ) are characterized at 700 °C with humid (3 vol %  $\text{H}_2\text{O}$ )  $\text{H}_2$  and ambient air as fuel and oxidant,

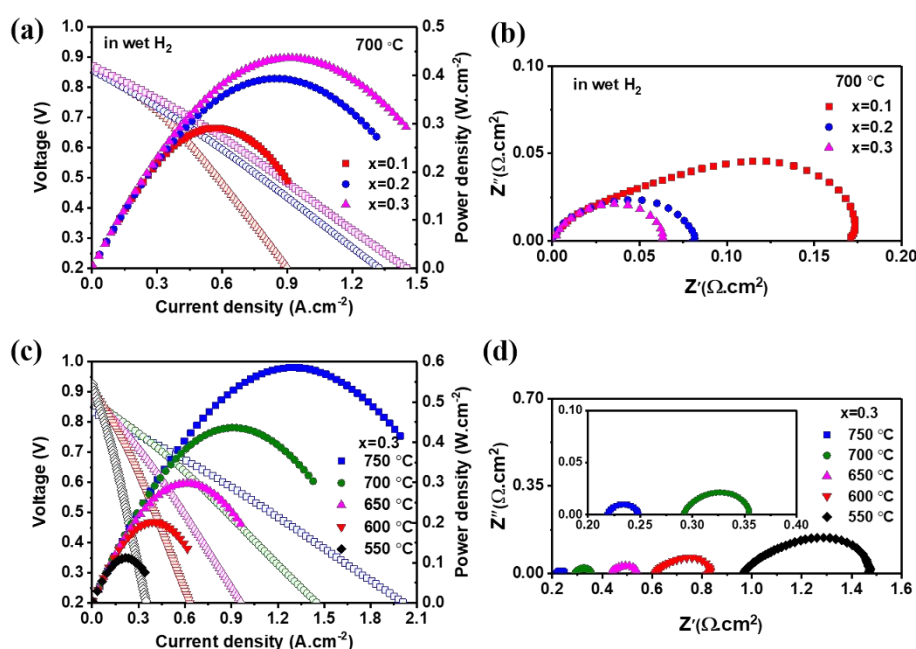


Figure. 8 (a) I-V and I-P curves and (b) EIS of SDC electrolyte-supported single cells PBFMNix-SDC|SDC|LSCF-SDC ( $x=0.1, 0.2, 0.3$ ) operating in humid  $\text{H}_2$  at 700 °C; (c) I-V and I-P curves and (d) EIS of SDC electrolyte-supported single cell PBFMNi0.3-SDC|SDC|LSCF-SDC operating in humid  $\text{H}_2$ .

respectively. Electrochemical impedance spectra (EIS) of these fuel cells are measured accordingly. The ohmic resistances of the electrolyte are subtracted from the impedance spectra to have a comparison of Ni-doping impact on the electrode polarization. As shown in Figure. 8a, b and Figure. S5, the peak power densities of the cells increase and the polarization resistances ( $R_p$ ) decrease with Ni contents increasing in anodes, indicating that the increase of Ni contents can largely accelerate anode reactions and may be partially attribute to the increased amounts of  $\text{FeNi}_3$  alloy nano-particles in reduced-PBFMNi0.3 for its strong catalytic activities toward fuel oxidation reactions. This is in good accordance with the above ECR results (Figure. 7). SDC electrolyte-supported single cells using PBFMNi0.3-SDC anode have achieved excellent electrochemical performance, as shown in Figure. 8c and d, with the peak power densities of 588, 437 and 297  $\text{mW}\cdot\text{cm}^{-2}$  at 750, 700 and 650 °C, respectively. It is comparable to famous  $\text{Sr}_2\text{FeMo}_{0.65}\text{Ni}_{0.35}\text{O}_{3-\delta}$  anode reported previously (590  $\text{mW}\cdot\text{cm}^{-2}$  at 750 °C). The corresponding  $R_p$  values are 0.028, 0.061, 0.149  $\Omega\cdot\text{cm}^2$  at 750, 700, 650 °C, respectively, much lower than other single cells with nano-catalysts decorated Fe-based oxide anodes like  $\text{La}_{0.8}\text{Sr}_{1.2}\text{Fe}_{0.9}\text{Co}_{0.1}\text{O}_{4\pm\delta}$  (0.550  $\Omega\cdot\text{cm}^2$  at 750 °C)<sup>42</sup>,  $\text{La}_{0.7}\text{Sr}_{0.3}\text{Fe}_{0.9}\text{Ni}_{0.1}\text{O}_{3-\delta}$  (0.403  $\Omega\cdot\text{cm}^2$  at 750 °C)<sup>43</sup>,  $\text{Sr}_2\text{Fe}_{1.5-x}\text{Mo}_{0.5x}\text{Ni}_x\text{O}_{6-\delta}$  (0.31  $\Omega\cdot\text{cm}^2$  at 750 °C)<sup>36</sup>,  $\text{Sr}_{0.95}\text{Ti}_{0.3}\text{Fe}_{0.63}\text{Ni}_{0.07}\text{O}_{3-\delta}$  (0.10  $\Omega\cdot\text{cm}^2$  at 800 °C)<sup>44</sup> as listed in table. 2. The good electrochemical performance of PBFMNi0.3 anode verifies its effectiveness in catalysing  $\text{H}_2$  oxidizing. Moreover, the cells using PBFMNi0.3 anode have reached a long term stable performance for 100 h in hydrogen with a constant current density of 200  $\text{mA}\cdot\text{cm}^{-2}$  applied (Figure. S6). Finally, multiple fuels, such as wet (10 vol %  $\text{H}_2\text{O}$ ) propane, wet (3 vol %  $\text{H}_2\text{O}$ ) syngas and syngas with 50 ppm  $\text{H}_2\text{S}$ , are injected to the anode side, respectively, to characterize the coking resistance and sulfur tolerance of the PBFMNi0.3 anode. The I-V and I-P curves of cells under these various fuels measured at 750 °C are plotted in Figure. 9a. When wet propane is used as the fuel, a cell displays a peak power density of 332  $\text{mW}\cdot\text{cm}^{-2}$ . Continuous and stable operation for

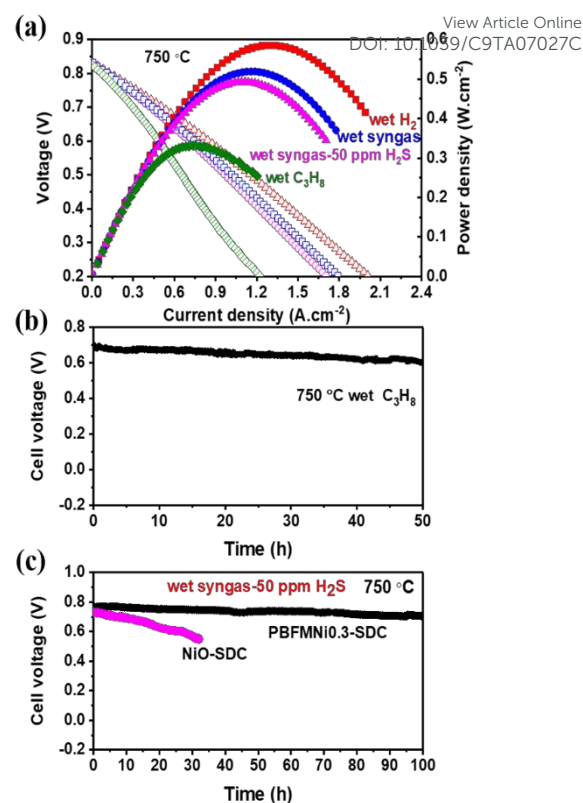


Figure. 9 (a) I-V and I-P curves of SDC electrolyte-supported single cells PBFMNi0.3-SDC|SDC|LSCF-SDC operating in wet  $\text{H}_2$ , wet propane, wet syngas and syngas-50 ppm  $\text{H}_2\text{S}$ , respectively, at 750 °C. Operating stability of the cells fuelled with (b) wet propane and (c) wet syngas with 50 ppm  $\text{H}_2\text{S}$  measured at 750 °C

Table. 2 Cell performance using metal nano-catalysts modified Fe-based perovskite anodes through in-situ reduction in humidified  $\text{H}_2$  fuel.

Anode composition	Electrolyte ( $\mu\text{m}$ )	Temperature (°C)	Peak power density ( $\text{mW}\cdot\text{cm}^{-2}$ )	$R_p$ ( $\Omega\cdot\text{cm}^2$ )	Reference
$\text{La}_{0.8}\text{Sr}_{1.2}\text{Fe}_{0.9}\text{Co}_{0.1}\text{O}_{4-\delta}$	LSGM (1000)	750	190	0.550	42
$\text{La}_{0.7}\text{Sr}_{0.3}\text{Fe}_{0.9}\text{Ni}_{0.1}\text{O}_{3-\delta}$	LSGM (300)	750	400	0.403	43
$\text{Sr}_2\text{FeMo}_{0.65}\text{Ni}_{0.35}\text{O}_{6-\delta}$	LSGM (300)	750	590	-	31
$\text{Sr}_2\text{Fe}_{1.4}\text{Mo}_{0.5}\text{Ni}_{0.1}\text{O}_{6-\delta}$	LSGM	750	380	0.31	36
$\text{Sr}_{0.95}\text{Ti}_{0.3}\text{Fe}_{0.63}\text{Ni}_{0.07}\text{O}_{3-\delta}$	LSGM (300)	800	950	0.10	44
$\text{Pr}_{0.6}\text{Sr}_{0.4}\text{Fe}_{0.7}\text{Ni}_{0.2}\text{Mo}_{0.1}\text{O}_{3-\delta}$	LSGM (300)	750	364	0.14	45
$\text{La}_{0.6}\text{Ca}_{0.4}\text{Fe}_{0.8}\text{Ni}_{0.2}\text{O}_{3-\delta}$ infiltrated SDC	SDC (300)	750	444	0.024	46
PBFMNi0.3-SDC	SDC (200)	750	588	0.028	This work

more than 50 hours (Figure. 9b) is achieved without observable degradation in performance, demonstrating its good carbon tolerance. When measured in humid syngas and syngas with 50 ppm H<sub>2</sub>S, the cells have achieved high performance of 520 and 498 mW·cm<sup>-2</sup> (Figure. 9a), respectively, and the polarization resistances of the cells are almost the same of 0.035 Ω·cm<sup>2</sup> (Figure. S7), slightly larger than that in humid H<sub>2</sub> (0.028 Ω·cm<sup>2</sup>). Such low polarization resistances greatly suggest the effectiveness of the anode toward syngas oxidation and especially the high sulphur tolerance. Yet, a slightly higher ohmic resistance in wet syngas-H<sub>2</sub>S is observed than that in wet syngas (Figure. S7), which may be attributed to the trace amount of sulfide (Ce<sub>2</sub>S<sub>3</sub>) on SDC particles as shown in the Figure. S9. Notably, the cell reaches a long-term stability for 100 h at 750 °C in wet syngas with 50 ppm H<sub>2</sub>S as shown in Figure. 9 c without obvious degradation. In contrast, a continuous decrease rates of 6 mV h<sup>-1</sup> in cell voltage is observed when NiO-SDC anode is exposed to the same fuel, indicating PBFMNi0.3 anode exhibits much better coking resistance and sulfur tolerance than conventional NiO-SDC anode in intermediate temperatures. After durability test in syngas with 50 ppm H<sub>2</sub>S, the microstructure of the porous PBFMNi0.3-SDC was examined and no carbon or carbon fibres can be observed (Figure. S10).

#### 4. Conclusions

In summary, we have explored a series of (PrBa)<sub>0.95</sub>Fe<sub>1.9-x</sub>Ni<sub>x</sub>Mo<sub>0.1</sub>O<sub>6-δ</sub> (PBFMNi<sub>x</sub>, x=0, 0.1, 0.2, 0.3) oxide anodes in IT-SOFCs. Firstly, pure perovskite phase PBFMNi0.3 can be synthesized in air without BaMoO<sub>4</sub> impurity and FeNi<sub>3</sub> alloy nano-particles were uniformly dispersed on the oxide surface under reducing atmosphere. Secondly, PBFMNi0.3 anode shown the biggest surface exchange coefficient of 3.25 × 10<sup>-4</sup> cm·s<sup>-1</sup> and the best electrochemical properties at 700 °C compared with PBFMNi0.1 and PBFMNi0.2, indicating that Ni-doping is beneficial to increase the catalytic activity of anode materials. Furthermore, electrolyte supported single cells with PBFMNi0.3 anode achieved very small polarization resistances of 0.028 Ω·cm<sup>2</sup> at 750 °C and the cells' peak power densities have reached 588, 520, 498 mW·cm<sup>-2</sup> in wet H<sub>2</sub>, wet syngas and syngas with 50 ppm H<sub>2</sub>S at 750 °C respectively. Moreover, the cells have kept long-term stability for 50 hours in wet propane and for 100 hours in wet syngas with 50 ppm H<sub>2</sub>S at 750 °C, which suggests the excellent coking resistance and sulfur tolerance of the PBFMNi0.3-SDC fuel electrode in IT-SOFCs.

#### Conflicts of interest

There are no conflicts to declare.

#### Acknowledgements

This work was financially supported by the National Key Research and Development Program of China (2017YFA0402800), the Natural Science Foundation of China (51872276), the External Cooperation Program of BIC, the Chinese Academy of Science (211134KYSB20130017), Hefei

Science Center CAS (2016HSC-IU004), and the Fundamental Research Funds for the Central Universities (WK340000004)

#### Notes and references

- 1 W. Wang, Y. Yang, D. Huan, L. Wang, N. Shi, Y. Xie, C. Xia, R. Peng and Y. Lu, *J. Mater. Chem. A*, 2019, **7**, 12538-12546.
- 2 S. C. Singhal and K. Kendall, *High-temperature solid oxide fuel cells: fundamentals, design and applications*, Elsevier, 2003.
- 3 M. Zhi, X. Chen, H. Finkler, I. Celik and N. Wu, *J. Power Sources*, 2008, **183**, 485-490.
- 4 Y. Jiang and A. Virkar, *J. Electrochem. Soc.*, 2003, **150**, A942-A951.
- 5 X. Ye, B. Huang, S. Wang, Z. Wang, L. Xiong and T. Wen, *J. Power Sources*, 2007, **164**, 203-209.
- 6 J. Liu and S. A. Barnett, *Solid State Ionics*, 2003, **158**, 11-16.
- 7 Y. Membrez and O. Bucheli, *J. Power Sources*, 2004, **127**, 300-312.
- 8 S. Baron, N. Brandon, A. Atkinson, B. Steele and R. Rudkin, *J. Power Sources*, 2004, **126**, 58-66.
- 9 A. Lussier, S. Sofie, J. Dvorak and Y. Idzerda, *Int. J. Hydrogen Energy*, 2008, **33**, 3945-3951.
- 10 S. Zha, Z. Cheng and M. Liu, *J. Electrochem. Soc.*, 2007, **154**, B201 B206.
- 11 E. D. Wachsman and K. T. J. S. Lee, *Science*, 2011, **334**, 935-939.
- 12 J. A. Kilner and M. Burriel, *Annu. Rev. Mater. Res.*, 2014, **44**, 365-393.
- 13 K. Sasaki, K. Susuki, A. Iyoshi, M. Uchimura, N. Imamura, H. Kusaba, Y. Teraoka, H. Fuchino, K. Tsujimoto and Y. Uchida, *J. Electrochem. Soc.*, 2006, **153**, A2023-A2029.
- 14 Y. Matsuzaki and I. Yasuda, *Solid State Ionics*, 2000, **132**, 261-269.
- 15 D. M. Bastidas, S. Tao and J. T. Irvine, *J. Mater. Chem.*, 2006, **16**, 1603-1605.
- 16 D. E. Fowler, J. M. Haag, C. Boland, D. M. Bierschenk, S. A. Barnett and K. R. Poeppelmeier, *Chem. Mater.*, 2014, **26**, 3113-3120.
- 17 K. B. Yoo and G. M. Choi, *Solid State Ionics*, 2011, **192**, 515-518.
- 18 G. Xiao and F. Chen, *Electrochem. Commun.*, 2011, **13**, 57-59.
- 19 M. Li, B. Hua, Y. Zeng, B. Shalchi Amirkhiz and J.-L. Luo, *J. Mater. Chem. A*, 2018, **6**, 15377-15385.
- 20 S. Sengodan, S. Choi, A. Jun, T. H. Shin, Y.-W. Ju, H. Y. Jeong, J. Shin, J. T. S. Irvine and G. Kim, *Nat. Mater.*, 2014, **14**, 205.
- 21 B. D. Madsen, W. Kobsiriphat, Y. Wang, L. D. Marks and S. Barnett, *ECS Trans.*, 2007, **7**, 1339-1348.
- 22 X. Lu, Y. Yang, Y. Ding, Y. Chen, Q. Gu, D. Tian, W. Yu and B. Lin, *Electrochim. Acta*, 2017, **227**, 33-40.
- 23 N. Monteiro, F. Noronha, L. Da Costa, M. Linardi and F. Fonseca, *Int. J. Hydrogen Energy*, 2012, **37**, 9816-9829.
- 24 N. Wu, W. Wang, Y. Zhong, G. Yang, J. Qu and Z. Shao, *ChemElectroChem*, 2017, **4**, 2378-2384.
- 25 O. Kwon, K. Kim, S. Joo, H. Y. Jeong, J. Shin, J. W. Han, S. Sengodan and G. Kim, *J. Mater. Chem. A*, 2018, **6**, 15947-15953.
- 26 Y. F. Sun, Y. Q. Zhang, J. Chen, J. H. Li, Y. T. Zhu, Y. M. Zeng, B. S. Amirkhiz, J. Li, B. Hua and J. L. Luo, *Nano Lett*, 2016, **16**, 5303-5309.
- 27 C. Yang, Z. Yang, C. Jin, G. Xiao, F. Chen and M. Han, *Adv. Mater.*, 2012, **24**, 1439-1443.
- 28 F. Liu, L. Zhang, G. Huang, B. Niu, X. Li, L. Wang, J. Zhao and Y. Jin, *Electrochim. Acta*, 2017, **255**, 118-126.
- 29 M. Li, Y. Ren, Z. Zhu, S. Zhu, F. Chen, Y. Zhang and C. Xia, *Electrochim. Acta*, 2016, **191**, 651-660.

## ARTICLE

Journal Name

- 30 Y. Wang, H. Zhang, F. Chen and C. Xia, *J. Power Sources*, 2012, **203**, 34-41.
- 31 M. Li, Z. Sun, W. Yang, T. Hong, Z. Zhu, Y. Zhang, X. Wu and C. Xia, *Phys. Chem. Chem. Phys.*, 2016, **19**, 503-509.
- 32 Z. Du, H. Zhao, S. Yi, Q. Xia, Y. Gong, Y. Zhang, X. Cheng, Y. Li, L. Gu and K. Świerczek, *ACS Nano*, 2016, **10**, 8660-8669.
- 33 M. C. Biesinger, B. P. Payne, A. P. Grosvenor, L. W. Lau, A. R. Gerson and R. S. C. Smart, *Appl. Surf. Sci.*, 2011, **257**, 2717-2730.
- 34 D. Neagu, T. S. Oh, D. N. Miller, H. Menard, S. M. Bukhari, S. R. Gamble, R. J. Gorte, J. M. Vohs and J. T. S. Irvine, *Nat Commun*, 2015, **6**, 8120.
- 35 G. Xiao, C. Jin, Q. Liu, A. Heyden and F. Chen, *J. Power Sources*, 2012, **201**, 43-48.
- 36 J. Feng, G. Yang, N. Dai, Z. Wang, W. Sun, D. Rooney, J. Qiao and K. Sun, *J. Mater. Chem. A*, 2014, **2**, 17628-17634.
- 37 Y. Li, B. Hu, C. Xia, W. Q. Xu, J. P. Lemmon and F. Chen, *J. Mater. Chem. A*, 2017, **5**, 20833-20842.
- 38 L. Zhang, Q. Zhou, Q. He and T. He, *J. Power Sources*, 2010, **195**, 6356-6366.
- 39 W. C. Chueh, Y. Hao, W. Jung and S. M. *Nat. Mater.*, Haile, 2012, **11**, 155.
- 40 L. Van der Haar, M. Den Otter, M. Morskate, H. J. Bouwmeester and H. Verweij, *J. Electrochem. Soc.*, 2002, **149**, J41-J46.
- 41 M. Zheng, J. Gao and C. Xia, *Solid State Ionics*, 2018, **319**, 92-97.
- 42 J. Zhou, T.-H. Shin, C. Ni, G. Chen, K. Wu, Y. Cheng and J. T. Irvine, *Chem. Mater.*, 2016, **28**, 2981-2993.
- 43 L. Bian, C. Duan, L. Wang, R. O'Hayre, J. Cheng and K. C Chou, *J. Mater. Chem. A*, 2017, **5**, 15253-15259.
- 44 T. Zhu, H. E. Troiani, L. V. Mogni, M. Han and S. A. Barnett, *Joule*, 2018, **2**, 478-496.
- 45 X. Lu, Y. Yang, Y. Ding, Y. Chen, Q. Gu, D. Tian, W. Yu and B. Lin, *Electrochim. Acta*, 2017, **227**, 33-40.
- 46 G. Yang, C. Su, Y. Chen, M. O. Tadé and Z. Shao, *J. Mater. Chem. A*, 2014, **2**, 19526-19535.

View Article Online  
DOI: 10.1039/C9TA07027C

PBFMNi<sub>0.3</sub> perovskite with *in-situ* exsolved FeNi<sub>3</sub> nano-catalysts is a promising carbon and sulfur tolerant anode for IT-SOFCs. View Article Online  
DOI: 10.1039/C9TA07027C

